Bussey et al. *EPJ Quantum Technology* (2024) 11:77
https://doi.org/10.1140/epjqt/s40507-024-00291-5

EPJ Quantum Technology
a SpringerOpen Journal

RESEARCH Open Access

# Numerical model of N-level cascade systems for atomic Radio Frequency sensing applications

Liam W. Bussey[1,2*], Yogeshwar B. Kale[2*], Samuel Winter[1], Fraser A. Burton[1], Yu-Hung Lien[2], Kai Bongs[4] and Costas Constantinou[3]

*Correspondence:
lwb149@student.bham.ac.uk;
y.kale@bham.ac.uk
[1]Applied Research, British Telecommunications, Adastral Park, Ipswich, IP5 3RE, Suffolk, UK
[2]School of Physics and Astronomy, University of Birmingham, Edgbaston Park, Birmingham, B15 2TT, UK
Full list of author information is available at the end of the article

**Abstract**

A ready-to-use numerical model has been developed for the atomic ladder (cascade) systems which are widely exploited in Rydberg Radio Frequency (RF) sensors. The model has been explicitly designed for user convenience and to be extensible to arbitrary N-level non-thermal systems. The versatility and adaptability of the model is validated up to 4-level atomic systems by direct comparison with experimental results from the prior art. The numerical model provides a good approximation to the experimental results and provides experimentalists with a convenient ready-to-use model to optimise the operation of an N-level Rydberg RF sensor. Current sensors exploit the 4-level atomic systems based on alkali metal atoms which require visible frequency lasers and these can be expensive and also suffer from high attenuation within optical fiber. The ability to quickly and simply explore more complex N-level systems offers the potential to use cheaper and lower-loss near-infrared lasers.

**Keywords:** Rydberg Atom-based Metrology; Numerical model; Simulation; RF Sensing

## 1 Introduction

Recent developments in atom-based quantum sensing have received considerable attention with development of commercial gravitational sensing, magnetometer, and Rydberg Radio Frequency (RF) sensors. Rydberg RF sensors have been shown to be International System of Units (SI) traceable and provide a self-calibrated solution for electrometers [1]. Further to the electrometers Rydberg sensors have been used for RF, mm Wave imaging [2] and Wireless communications [3].

Over the last decade atom-based RF electrometers have been shown to be capable of working over a wide range of frequencies [4–6] with self-calibration to atomic energy levels allowing for precision measurements. Further interest has been sparked in these receivers due to the sensitivity improvement in comparison to traditional dipole antennas [7–9]. This potential for an increase in sensitivity below that of the thermal noise floor has gained interest from communication engineers with a new focus on atom-based RF communication using both analogue and digital encoding [3, 10–12]. Furthermore, this

technology has been developed for the purpose of RF imaging in the terahertz regime [2, 13], with applications ranging from building inspection to RF environment tracking. Both the amplitude and phase of a weakly modulated RF field [3, 14] can be detected at higher modulation rates limited only by the relaxation time of the atom. This limitation can be improved upon by using multiple optical beam paths through the vapor cell or multiple receiver cells [15]. The detection sensitivity can be improved by controlling laser stability in terms of laser frequency locking and laser linewidth, together with using low noise photodiodes, and using homodyne [16] and heterodyne [17] detection methods. The state-of-the-art atomic sensors, RF sensitivity is a rapidly evolving field with sensitivity ranging from 3 $\mu$V/cm/$\sqrt{\text{Hz}}$ [18] down to 55 nV/cm/$\sqrt{\text{Hz}}$ [17] and a theoretical limit of 100 pV/cm/$\sqrt{\text{Hz}}$ [18–20] for a variety of radio frequencies.

Although greater sensitivity can be achieved there is a trade-off with the RF modulation rate [7, 21]. Other methods have also been researched for further enhancing the sensitivity of these sensors such as using a split ring resonator [22]. This has displayed a two-fold increase in sensitivity of the system.

This type of atom-based RF sensor exploits the properties of highly excited states in alkali and alkaline-earth metallic vapor [23, 24] such as Rubidium (Rb) and Strontium (Sr). To make Rb vapor sensitive to externally applied RF fields, the atomic system is prepared by moving the valence electron from the ground state to the Rydberg state using an optical two-photon transition. Once the two-photon transition has occurred, the atomic medium which is opaque to the first optical transition is rendered transparent using the second optical photon through the non-linear quantum optical effect of Electromagnetically Induced Transparency (EIT) [25–27]. With the atomic system in the Rydberg state, Autler-Townes (AT)-splitting [28–30] is exhibited when a resonant RF field is presented to the system. This splitting takes the second optical absorption off-resonance and causes electrons in the first excited state to decay back to the ground state to be re-absorbed.

In this work, numerical modelling of this complex system of atomic interactions is performed by using Python modules such as QuTiP [31] and ARC (Atomic Rydberg Calculator) [32, 33] to obtain an accurate absorption spectrum for different parameter sweeps.

This paper comprises five sections: Sect. 2 describes the analytical model for a four-level cascade system which is used to build the generic numerical model described in Sect. 3. The model accepts the necessary information about the desired atomic system under consideration such as transitions involved, Rabi frequencies, RF parameters, etc. The results in Sect. 4 versatility of our model by validating it with the Cs and Rb atomic systems. The results are further expanded by including other broadening mechanisms described in Sect. 2 which increase the complexity of the model to solve analytically but can be implemented simply into the numerical model. This allows for the results section to cover a range of parameter sweeps and show the impact this has on the capability of the RF sensor. Section 5 gives our concluding remarks and further work planned to expand the capabilities of this model.

## 2 Theory

This section discussed the analytical approach to solve the master equation for a 4-level cascade system. A typical experimental setup for such sensors is shown in Fig. 1 A) and corresponding energy level structure is in Fig. 1 B). These equations can easily be adapted to different experimental configurations such as Lambda, Vee, and Inverted-Y [34] scheme

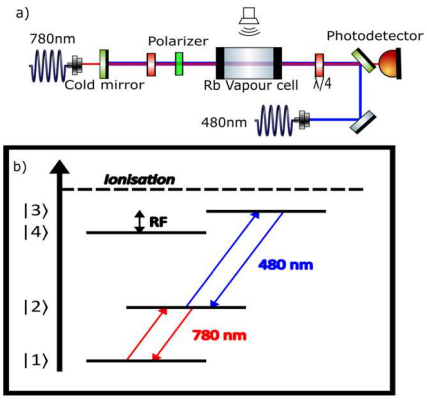


**Figure 1** A) Shows a typical rubidium experimental set-up for using EIT for electric field sensing. B) Shows a generalised ladder system for Rubidium, which is used to develop the theoretical model and show the interactions between the states. Here the probe wavelength is 780 nm, and the coupling laser wavelength is 480 nm

with suitable modifications in the interaction Hamiltonian. The analytical solution developed in this section is used to develop a Python-based numerical model in Sect. 3.

## 2.1 The master equation

The master equation shown in Equation (1) is used to describe the interactions and dynamics of the 4-level atomic system shown in Fig. 1 B). This equation is employed to describe the time evolution of the atomic system in a probabilistic combination of states in which the electron undergoes transitions between various atomic states. This represents a solution to the Schrödinger equation.

$$\dot{\rho} = \frac{-i}{\hbar}[H, \rho] - \mathcal{L}_i(\rho) \tag{1}$$

Here, $\rho$ is the density matrix for our four-level ladder system, H is the interaction Hamiltonian and $\mathcal{L}_i(\rho)$ is the Lindblad super-operator which contains information on the dephasing and broadening mechanisms involved. Using the rotating wave approximation (RWA) [35] which is a change in bases to eliminate both time and phase components of the Hamiltonian. The Hamiltonian is simplified to the matrix shown in Equation (2).

$$H = \frac{-\hbar}{2}\begin{bmatrix} 0 & \Omega_p & 0 & 0 \\ \Omega_p & -2\Delta_p & \Omega_c & 0 \\ 0 & \Omega_c & -2(\Delta_p + \Delta_c) & \Omega_{rf} \\ 0 & 0 & \Omega_{rf} & -2(\Delta_p + \Delta_c + \Delta_{rf}) \end{bmatrix} \tag{2}$$

The Hamiltonian shown in Equation (2) describes a system of interaction where transition can only occur between energy levels. i.e. $|1\rangle \rightleftharpoons |2\rangle$, $|2\rangle \rightleftharpoons |3\rangle$ and $|3\rangle \rightleftharpoons |4\rangle$. Further to this these transition must obey Hund's rules. In Equation (2), the off-diagonal elements $\Omega_{p,c,rf}$ are the Rabi frequency for a given transition and the $\Delta_{p,c,rf}$ are the interaction dephasing from the resonance of the transition. From Equation (1) $\mathcal{L}_i(\rho)$ can further be described as,

$$\mathcal{L}_i(\rho) = \mathcal{L}_{spon} + \mathcal{L}_{laser} \tag{3}$$

Here, $\mathcal{L}_{spon}$ is Einstein A coefficient damping (also known as the spontaneous decay), $\mathcal{L}_{laser}$ is the dampening caused by the laser linewidth [36]. Their corresponding matrices

are shown in equations (4) & (5).

$$\mathcal{L}_{spon} = \begin{bmatrix} -A_2\rho_{22} & \frac{A_2\rho_{12}}{2} & \frac{A_3\rho_{13}}{2} & \frac{A_4\rho_{14}}{2} \\ \frac{A_2\rho_{21}}{2} & A_2\rho_{22} - A_3\rho_{33} & \frac{(A_2+A_3)\rho_{23}}{2} & 0 \\ \frac{A_3\rho_{31}}{2} & \frac{(A_2+A_3)\rho_{32}}{2} & A_3\rho_{33} - A_4\rho_{44} & \frac{(A_3+A_4)\rho_{34}}{2} \\ \frac{A_4\rho_{41}}{2} & 0 & \frac{(A_4+A_3)\rho_{43}}{2} & A_4\rho_{44} \end{bmatrix} \tag{4}$$

$$\mathcal{L}_{laser} = \begin{bmatrix} 0 & \gamma_p\rho_{12} & (\gamma_p+\gamma_c)\rho_{13} & (\gamma_p+\gamma_c+\gamma_{rf})\rho_{14} \\ \gamma_p\rho_{21} & 0 & \gamma_c\rho_{23} & (\gamma_c+\gamma_{rf})\rho_{24} \\ (\gamma_p+\gamma_c)\rho_{31} & \gamma_c\rho_{32} & 0 & \gamma_{rf}\rho_{34} \\ (\gamma_p+\gamma_c+\gamma_{rf})\rho_{41} & (\gamma_c+\gamma_{rf})\rho_{42} & \gamma_{rf}\rho_{34} & 0 \end{bmatrix} \tag{5}$$

In Equation (4), $A_{ij}$ is the Einstein A coefficient for level transition between the i and j states. Note that the zero value are due to dipole forbidden transitions. In Equation (5), $\gamma_{p,c,rf}$ are the respective laser linewidths. This equation can be simplified by setting $\gamma_{rf}$ to zero as the RF field doesn't not have an associated linewidth.

## 2.2 The steady state solution

To solve for the steady state, the density matrix equation can be written as a set of 10 linear equations. For ease of the derivation we have only considered the case where the Lindblad Super-operator contains information on the Einstein A coefficient.

$$\begin{aligned}
\dot{\rho_{1,1}} &= \frac{i\Omega_p}{2}(\rho_{21} - \rho_{12}) + A_2\rho_{22} \\
\dot{\rho_{2,2}} &= \frac{i\Omega_p}{2}(\rho_{12} - \rho_{21}) + \frac{i\Omega_c}{2}(\rho_{32} - \rho_{23}) - A_2\rho_{22} + A_3\rho_{33} \\
\dot{\rho_{3,3}} &= \frac{i\Omega_{rf}}{2}(\rho_{43} - \rho_{34}) + \frac{i\Omega_c}{2}(\rho_{23} - \rho_{32}) + A_4\rho_{44} - A_3\rho_{33} \\
\dot{\rho_{4,4}} &= \frac{i\Omega_{rf}}{2}(\rho_{34} - \rho_{43}) - A_4\rho_{44} \\
\dot{\rho_{1,2}} &= \frac{i\Omega_p}{2}(\rho_{22} - \rho_{11}) + (i\Delta_P - \frac{A_2}{2})\rho_{12} - \frac{i\Omega_c}{2}\rho_{13} \\
\dot{\rho_{1,3}} &= \frac{i\Omega_p}{2}(\rho_{23}) + (i(\Delta_P + \Delta_C) - \frac{A_3}{2})\rho_{13} - \frac{i\Omega_c}{2}\rho_{12} - \frac{i\Omega_{rf}}{2}\rho_{14} \\
\dot{\rho_{1,4}} &= \frac{i\Omega_p}{2}(\rho_{24}) + (i(\Delta_P + \Delta_C + \Delta_{rf}) - \frac{A_4}{2})\rho_{14} - \frac{i\Omega_{rf}}{2}\rho_{13} \\
\dot{\rho_{2,3}} &= \frac{i\Omega_p}{2}(\rho_{13}) + (i\Delta_C - \frac{(A_2+A_3)}{2})\rho_{23} - \frac{i\Omega_{rf}}{2}\rho_{24} + \frac{i\Omega_c}{2}(\rho_{33} - \rho_{22}) \\
\dot{\rho_{2,4}} &= \frac{i\Omega_p}{2}(\rho_{14}) + (i(\Delta_C + \Delta_{rf}))\rho_{24} - \frac{i\Omega_{rf}}{2}\rho_{23} + \frac{i\Omega_c}{2}(\rho_{34}) \\
\dot{\rho_{3,4}} &= \frac{i\Omega_c}{2}(\rho_{24}) + (i\Delta_{rf} - \frac{A_3+A_4}{2})\rho_{34} + \frac{i\Omega_{rf}}{2}(\rho_{44} - \rho_{33})
\end{aligned} \tag{6}$$

The equation shown in (6) can be simplified further for the system by assuming that all the population is initially in state $|1\rangle$ i.e. ground state thus, $\rho_{11} \approx 1$ and $\rho_{22} \approx \rho_{33} \approx \rho_{44} \approx 0$. By using the weak probe approximation, all terms which are proportional to $\Omega_p^2$ can be dropped out. If one applies the steady state approximation, the left-hand side of the equations in (6) can be set to zero. It is possible to then find $\dot{\rho}_{24}$ and $\dot{\rho}_{23}$ are equal to zero as

these equations are linearly proportional to $\Omega_p$. This leaves 3 linear equations of motion which can be solved numerically or analytically. To solve these analytically the next step is to write these 3 linear equations in matrix form shown in Equation (7) and solve them for the steady state.

$$\begin{bmatrix} \dot{\rho}_{1,2} \\ \dot{\rho}_{1,3} \\ \dot{\rho}_{1,4} \end{bmatrix} = \begin{bmatrix} (i\Delta_P - \frac{A_2}{2}) & -\frac{i\Omega_c}{2} & 0 \\ -\frac{i\Omega_c}{2} & i(\Delta_P + \Delta_C) - \frac{A_3}{2} & -\frac{i\Omega_{rf}}{2} \\ 90 & -\frac{i\Omega_{rf}}{2} & i(\Delta_P + \Delta_C + \Delta_{rf}) - \frac{A_2+A_4}{2} \end{bmatrix} \begin{bmatrix} \rho_{12} \\ \rho_{13} \\ \rho_{14} \end{bmatrix} + \begin{bmatrix} \frac{-i\Omega_p}{2} \\ 0 \\ 0 \end{bmatrix} \tag{7}$$

By setting the time derivative of the density matrix element equal to zero (left hand side) of Equation (7), it is then possible to solve these three linear equations of motion for the steady state in terms of the density matrix elements.

The next step is to determine which of these 3 linear equations yield the required information relating to the macroscopic and microscopic electric susceptibility. This is determined by taking the partial trace of the density matrix multiplied by the dipole operator matrix shown in Equation (8).

$$\mathrm{Tr}\{\rho\wp\} = \mathrm{Tr}\left\{ \begin{bmatrix} \rho_{11} & \rho_{12} & \rho_{13} & \rho_{14} \\ \rho_{21} & \rho_{22} & \rho_{23} & \rho_{24} \\ \rho_{31} & \rho_{32} & \rho_{33} & \rho_{34} \\ \rho_{41} & \rho_{42} & \rho_{43} & \rho_{44} \end{bmatrix} \begin{bmatrix} 0 & \wp_{12} & 0 & 0 \\ \wp_{21} & 0 & \wp_{23} & 0 \\ 0 & \wp_{32} & 0 & \wp_{34} \\ 0 & 0 & \wp_{43} & 0 \end{bmatrix} \right\} \tag{8}$$

$$= \rho_{12}\wp_{21} + \rho_{21}\wp_{12} + \rho_{23}\wp_{32} + \rho_{32}\wp_{23} + \rho_{34}\wp_{43} + \rho_{43}\wp_{34}$$

Using the solution to Equation (8), and the definition of the electric susceptibility come the relation of the macroscopic and microscopic description of the dielectric polarization of the system [37], this allows us to write the analytical solution shown by Equation (9).

$$\chi = \frac{2N \mid \wp_{12} \mid}{E_P \epsilon_0} \rho_{12} \tag{9}$$

The result shown in Equation (9) can be broken into the real and imaginary components, where the real part describes the dispersion of the vapor, and the imaginary part is proportional to the absorbance of the vapor. $\rho_{12}$ is the density matrix element between the ground state and the first excited state, so it describes the interaction of the atomic medium with the probe laser. The probe laser excites the valence electron from the ground state to the first excited state and is absorbed in the process. So a measurement of changes in the probe absorption profile scales directly with $\rho_{12}$. Assuming a narrow probe linewidth and a low probe power, there will be negligible interactions between the atomic ground state and higher level excited states so only $\rho_{12}$ will drive the atomic medium's susceptibility. N is the number of atoms involved in the interaction area. $\mid \wp_{12} \mid$ is the magnitude of the dipole moment. $E_p$ is the field strength of the probe. $\epsilon_0$ is the permittivity of free space. Finally, $\rho_{12}$ is used to describe the steady state solution in equation (7).

To convert absorbance to transmittance, the Beers absorption coefficient [38] is used for the probe laser, shown in Equation (10).

$$\alpha = \frac{2\pi \, \mathrm{Im}\{\chi\}}{\lambda_p} \tag{10}$$

where $\lambda_p$ is the wavelength of the probe laser and $\mathrm{Im}\{\chi\}$ is the imaginary component of the electric susceptibility.

## 3 Numerical model and python packages

In recent years Python packages for more specialised scientific computing have been developed in parallel to the work presented in this paper. This work allows users to perform complex calculations and model parameters such as electric susceptibility in an atomic vapour [39]. An example of the toolboxes available to solve some of these light-atom interactions are QuTiP [30, 31], mbsolve [40], MaxwellBloch [41] and Simple Python tools for modelling few-level atom-light interactions [42]. Our numerical model differs from the work shown in [42] by providing a ready made software toolkit for users which builds on the work presented in their paper. To further distinguish this work, our numerical model is suitable for the study of an arbitrary N-level system. The work presented in this gitlab [43] is specific to Rubidium 87 in a lambda configuration for study of the zeeman splitting in an optical cavity, whereas our numerical model is designed for ladder configurations in N level systems. This work presented in [44] considers the population dynamic in a fixed 4 level scheme when considering a pulsed laser whereas our work assumes a continuous wave system in the steady state.

Due to the complexity of the equations presented in Sect. 2, it becomes increasingly difficult to solve analytically for systems that extend above 4 atomic energy levels and when the dephasing mechanism becomes more complex, even when using assumptions to simplify the system of equations. Using the equations presented in Sect. 2, the numerical model is built with the aim of being able to analyse multi-level systems with complex dephasing mechanisms for a range of atom-based RF sensors.

The numerical model uses a combination of Python libraries to calculate the electric susceptibility. For this paper, the ARC (Atomic Rydberg Calculator), QuTip, NumPy [45] and SciPy [46] are used together with custom scripts to take user information on the system configuration.

First, to build a numerical model that can study multiple atoms and energy level configurations, a method of acquiring and storing information from the user is required. Using the equations presented in Sect. 2, the numerical model needs the following inputs from the user, which will be used to extract the relevant data from the ARC to be processed using QuTiP: The numerical model requires information on the number of energy levels in the system, the principal quantum number for each state $n$, the quantum number of the angular momentum $l$, the total angular momentum $J$, and the projection of the total angular momentum $m_j$ along the $z$ axis. Next, the user needs to define what type of interaction is occurring between each transition, this could be either a laser or RF interaction. If the field is a laser interaction, then the following information is required: the power of laser field in mW, the beam waist, the polarisation of the field, whether the field is on-resonance, if the field is scanning, dephasing scan range and the laser linewidth in kHz if applicable. If the field is RF, then: the strength of the electric field in $V/m$, the polarisation

```
    def get_rabi(atom_list: list[arc.Rubidium85], feild: str, n1: int, l1: int, j1:
     float, mj1: float, n2: int, l2: int, j2: float, q: int, p: float, w: float,
    p_rf: float, linewidth: float) ->list[float]:
    """Gets the Rabi Frequency for the defined tranision using ARC `
    getRabiFrequency` or `getRabiFrequency2`

    Args:
        atom (list[arc.Rubidium85]): This is a list containing the ARC object of
    Rb85, but may contain any relevant atomic species. This must be an ARC atom
    class.
        feild (str):  If the field is a laser field 'L' this will use `
    getRabiFrequency` else it will use `getRabiFrequency2` for Radio frequency 'R'
        n1 (int): Lower principal quantum number.
        l1 (int): lower orbital angular momentum quantum number.
        j1 (float): lower total angular momentum.
        mj1 (float): lower second angular momentum number.
        n2 (int): Upper principal quantum number.
        l2 (int): Upper orbital angular momentum quantum number.
        j2 (float): Upper total angular momentum.
        q (int): The polarisation state of the field, from the set {-1, 0, 1}.
        p (float): The power of the laser beam in mW.
        w (float): The width of a laser beam in um.
        p_rf (float):Field strength of an RF wave, in V m^(-1).
        linewidth (float): laser linewidth. not used in this function

    Returns:
        list[float]: Returns the rabi frequency for a given transition in rad s
    ^(-1)
    """
    if (feild == 'L'):

        return [(atom_list[i].getRabiFrequency(n1, l1, j1, mj1,
                                               n2, l2, j2,
                                               q, p, w)) for i in range(len(
    atom_list))]


    else:

        return [(atom_list[i].getRabiFrequency2(n1, l1, j1, mj1,
                                               n2, l2, j2,q,
                                               p_rf)) for i in range(len(
    atom_list))]
```

**Figure 2** This show how the information on the transition states taken from the user is then used to calculate the Rabi frequency for either as laser or RF field by interfacing with ARC

of the field, whether the field is on resonance, if the field is scanning, and finally upper and lower dephasing values.

Using the information provided above, the numerical model extracts the required information from the ARC Libraries to form the Hamiltonian shown in Equation (2). The information needed to form the Hamiltonian is the Rabi frequency for each transition element in the off-diagonal elements. The Rabi frequency is calculated using information provided by the user by interfacing with the ARC Python libraries to retrieve this for each state, as shown in Fig. 2.

The retrieved value is converted from rad $s^{-1}$ to Hz. The value is then stored in a data frame ready for use, with the diagonal element being the laser or RF dephasing combined for each laser or RF frequency in the transition. If a transition is off resonance this would also appear in the diagonal term in the Hamiltonian.

Figure 3 shows an extract of the numerical model used to build the Hamiltonian given in Equation (2). The Hamiltonian builder can be used to generate an N-level ladder matrix based on the number of states and parameters provided by the user as described above.

As described in Sect. 2, the Hamiltonian only describes part of the process. It is necessary to add the dephasing mechanism. This is done by taking the information present in the Lindblad $\mathcal{L}_i(\rho)$ super-operator shown in equations (4) and (5) and forming them into the collapse operator which is used by the QuTiP steady-state solver. For a more detailed description of the collapse operator, please refer to QuTiP's API [47].

```python
def Hamil_builder(number_states: int, Trans_wave: pd.DataFrame, dephasing: list[
    float]) -> np.array:
    """This Function is used to build an NxN hamiltionian in cascade configuration,
     where N is the number_states in the atom. The off diagonal element discribe
    the jump operation using rabi frequency. the diagonal terms discribe the
    dephasing across the transition.

    Args:
        number_states (int): This is the interger value for the total number of
    atomic state in the system.
        Trans_wave (pd.DataFrame): Dataframe with the expanded information on the
    excitation pathway gathered using ARC
        dephasing (list[float]): This is a list of floats containing the dephasing
    scanning range and number of steps

    Returns:
        np.array: This 2D array contains the an nxn Hamiltionian
    """
    Hamiltonian = np.zeros(shape=((number_states),(number_states)))
         ### NxN matrix of zeros to form the base Hamiltonian


#### how to build this a function builder
    for i in range (number_states- 1):

        Hamiltonian[i][i+1] = -(1/(4*np.pi))*(Trans_wave.iloc[i]['rabi Freq rads/s'
    ])   ### fills the upper off diagonal element for an NXN matrix
        Hamiltonian[i+1][i] = -(1/(4*np.pi))*(Trans_wave.iloc[i]['rabi Freq rads/s'
    ])   ### fills the lower off diagonal element for an NXN matrix

    for i in range (number_states):
        if i == 0:
            Hamiltonian[i][i] = 0.0
        else:
            Hamiltonian[i][i] = dephasing[i-1]
           # forms the diagonal element of the system

    return(Hamiltonian)
```

**Figure 3** Show the extract of code used to form the Hamiltonian for a N level cascade system

The collapse operator has two components: the first comes from the Einstein A coefficient for the spontaneous emission of an electron from a given energy state. This is calculated by passing the required information on the atomic state through the ARC to calculate the transition rate. This is then passed into a N-by-N matrix with the transition rate for each transition occupying the element points shown in Equation (4). Figure 4 shows how this matrix is built within the numerical model.

When considering the theory shown in Sect. 2, the Lindblad super-operator can be expanded in the numerical model to include laser linewidth broadening as shown in Equation (5). To inculde this we implement the same matrix approach shown in Fig. 5 by using the information provided by the user at the input stage.

Having laid out the three main equations needed to run the numerical solver; the steady state solution is found using a LU decomposition through QuTiP's steady state solver. This solver uses the direct method of solving the steady state of the Hamiltonian, which requires a large system memory to solve. This is due to the reducing algorithm used in QuTiP to fill in the non-zero elements. Once the steady state for the system has been solved, more information on the transition of interest is required.

In most cases, the probe transition is from the ground to first excited state. The steady-state solution for all states is used and multiplies this by the atomic basis operator which describes which transition state is being considered. The final answer yields the complex electric susceptibility which contains information on the dispersion and absorbance shown in Equation (9).

To further expand this numerical model shown in the Additional file 1 to a higher order of N the user would need to changed the `number_state` parameter. This parameter is

```python
def collapse_op(number_state: float, basis: list[qp.Qobj], decay_wave: pd.DataFrame
    ) -> np.array :
    """Natrual Decay collapse operator

    Args:
        number_state (float): This is the interger value for the total number of
    atomic state in the system.
        basis (list[qp.Qobj]): List of N = number_states Fock states
        decay_wave (pd.DataFrame): This a Dataframe with the expanded information
    on the decay pathway gathered using ARC.

    Returns:
        np.array: This return an array of collapse operature generaterd using the
    natural decay taken from ARC
    """
    natural_line =[]
    for i in range(number_state - 1):
        #spontaneous decay in Hz
        natural_line.append((decay_wave.iloc[i]['Transition Rate (Hz) with BBR for
    Rb']))

    ls = []
    dim = number_state
    n_l = []

    for j in range(1, dim):
        op = np.zeros((dim, dim))
        natural_line_value = natural_line[j-1]

        op[j-1,j] = natural_line_value
        ls.append(op)

    ls = np.array(ls)

    return(ls)
```

**Figure 4** Show the method used to generate the collapse operator for the spontaneous emission Lindblad super operator

```python
 """Laser linewidth collapse operator, allow for the braodening of the transition
    based on the laser linewidth, this will set the RF linewidth to zero

    Args:
        number_state (float): This is the interger value for the total number of
    atomic state in the system.
        laser_trans (list[laser_parameter]): This is a list of field parameter
    object, all of the key experimental parameters are used here. These will also
    set the numerical 'experiment' parameters, e.g. which wavelengths are being
    scanned over.
        basis (list[qp.Qobj]): List of N = number_states Fock states
        Trans_wave (pd.DataFrame): This a Dataframe with the expanded information
    on the excitation pathway gathered using ARC.

    Returns:
        list: returns a list of collapse operator for the laser linewidth
    """
#laser linewidth in Hz
    laser_line =[]
    for i in range(number_state - 1):
        if  Trans_wave.iloc[i]['feild'] == 'R':
            laser_line.append(0)
        else:
            laser_line.append((Trans_wave.iloc[i]['linewidth']))
    ls = []
    dim = number_state
    q_l = []
    op = np.zeros((dim, dim))

    for j in range(1, dim):
        op = np.zeros((dim, dim))
        laser_line_value = laser_line[:j]
        laser_line_value.reverse()

        for i in range(0, j):
            op[i, j] = (np.sum(laser_line_value[:(j-i)]))

        ls.append(op)
    return ls
```

**Figure 5** Shows the numerical method for generating the laser linewidth collapse operator

an integer value for the total number of atomic states in the system. By changing this value the user would be required to supply additional information about the system.

## 4 Results and discussion

This section explores the results generated by the numerical model and compares them to published experimental data. To demonstrate the versatility and adaptability of the model, we will look at two different atomic species using different energy-level configurations in a cascade set up. For each atom, we will do a parameter sweep and show the effects changing one of the variables has on the operation and capability of the sensor.

It is assumed the user knows the quantum numbers of each atomic state of interest, i.e. $n$, $l$, $j$, and $m_j$. This data is used to create a `state_describing_object` that, when used in sequence, forms an excitation pathway. The order of the atomic states in the ladder scheme are fed in as a list into the `transition_generator_excitation` and `transition_generator_decay` functions. These yield two dataframes that contain the information that characterises all of the transitions in the ladder scheme, as calculated by ARC. The laser input data, namely the power, beam waist, linewidth, direction and polarisation is captured in a list formed from the instance of the `laser_params` class, with one other input that is the separation between the laser frequency and the resonant frequency of the targeted transition. This is set with an upper and lower bound that also dictates whether the parameter is swept through, or if they are equal, is held constant. The RF field is characterised similarly, however the beam waist and direction is not set for the model. Finally, the excitation and decay pathway dataframes, along with the laser and RF parameters, are passed to the `EIT_builder` function which produces the scanned frequencies, and a list of arrays that contain the electric susceptibilities of the ladder system at the desired wavelengths. This data is then plotted using any standard plotting library.

### 4.1 Transmission profiles for $^{133}$Cs

The numerical model is first validated against the experimental parameters from Rydberg Atom-based RF power measurements [48]. In this paper the Author chose to use $^{133}$Cs, targeting the following atomic transitions $6S_{1/2} \rightarrow 6P_{3/2} \rightarrow 35D_{5/2} \rightarrow 36P_{3/2}$. The probe laser used to excite the $6S_{1/2}$ to the $6P_{3/2}$ was operated at 3.2 $\mu$W with a beam diameter of 0.708 mm. The coupling laser operated in a counter-propagating set-up to the probe is used to move the electron from the $6P_{3/2}$ to the $35D_{3/2}$ with a laser power of 17.3 mW and a beam diameter of 0.708 mm. The final transition is an RF field coupled to the system at 17.86 GHz with a field strength of 0.75 V m$^{-1}$.

The section is split in to three. Section 4.1.1 will consider how changes in the Rabi frequency effect the System. Section 4.1.2 will look at how the laser linewidth broadening effects the sensor and Sect. 4.1.3 will look at how RF frequency detuning could increase the atomic RF sensor sensitivity for direct detection.

#### *4.1.1 Rabi frequency dependence on RF sensitivity*

When operating at or near saturation intensity, this should produce an absorption linewidth close to the D2 transition natural linewidth ($2\pi \times 5.2$ MHz [49]). As the probe power increases, the power broadening effect is observed; this causes an increase in the absorption linewidth. Figure 6 A) shows the power broadening effect using experimental parameters from [48] (solid black line) and simulating the increase of probe power. This

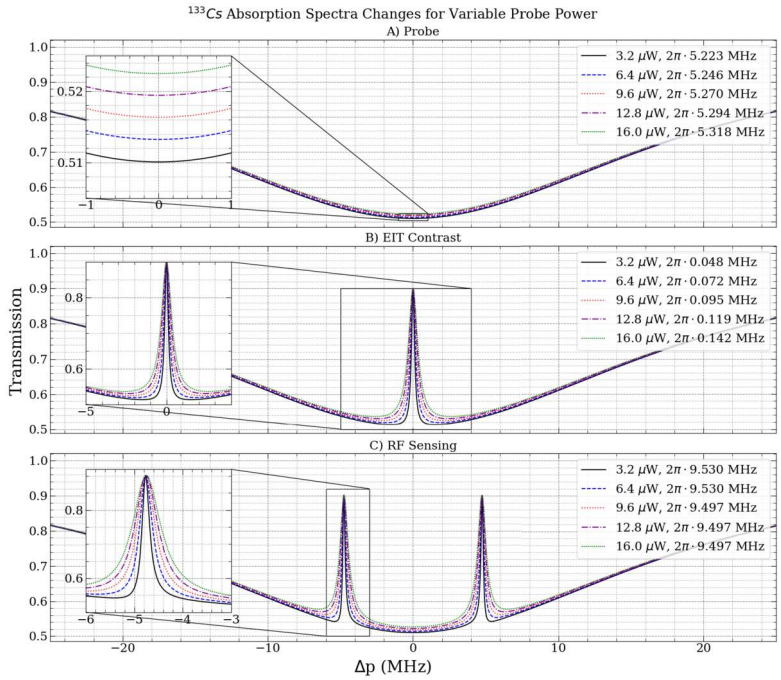


**Figure 6** A) Shows the effect of probe power on probe transmission spectra. B) EIT contrast as function of probe power (at constant coupling power of 17.3 mW). C) Show the effect changes in probe power has on the RF splitting (at constant coupling power of 17.3 mW and constant RF field strength at 0.75 V m$^{-1}$)

results in a broadening of the EIT contrast shown in 6 B) and a broadening in the splitting used for RF sensing shown in Fig. 10 C). If the RF field is significantly weaker or the power broadening is greater than this, then this causes a significant reduction in the sensitivity of the RF sensing when measuring the field strength.

Figure 6 C) shows the separation of the EIT peak into two peaks, due to Autler-Townes splitting. By measuring the separation of the two peaks it is possible to calculate the intensity of the applied RF field using Equation (11).

$$|E| = \frac{2\pi\hbar\lambda_p}{\wp_{rf}\lambda_c}\Delta f_m \tag{11}$$

The strength of the applied electric field is calculated from Equation (11).$\wp_{rf}$ is the dipole moment for the RF transition. $\hbar$ is the reduced planks constant. $\frac{\lambda_p}{\lambda_c}$ is the wavelength of the probe laser divided by the wavelength of the coupling laser. This is given the value of 1 for our system of study as we are not considering dipole shifting of the wavelength caused by a thermal system. When considering a thermal system this can also be set to 1 when the coupling laser is the laser being scanned. $\Delta f_m$ is the peak separation caused by the application of the electric field. In the example from Fig. 6 C) the splitting between the two peaks is approximately 9.53 MHz or 9.497 MHz for the stronger probe laser. The electric dipole moment for the RF transition is given as $994.18a_0$e where $a_0$ is the Bohr radius and e is the charge of an electron. Using the above values, the strength of the electric field is 0.749 V m$^{-1}$ or 0.747 V m$^{-1}$ both of which gives a very close approximation to the input field strength taken from the experimental paper [48] for this system. However,

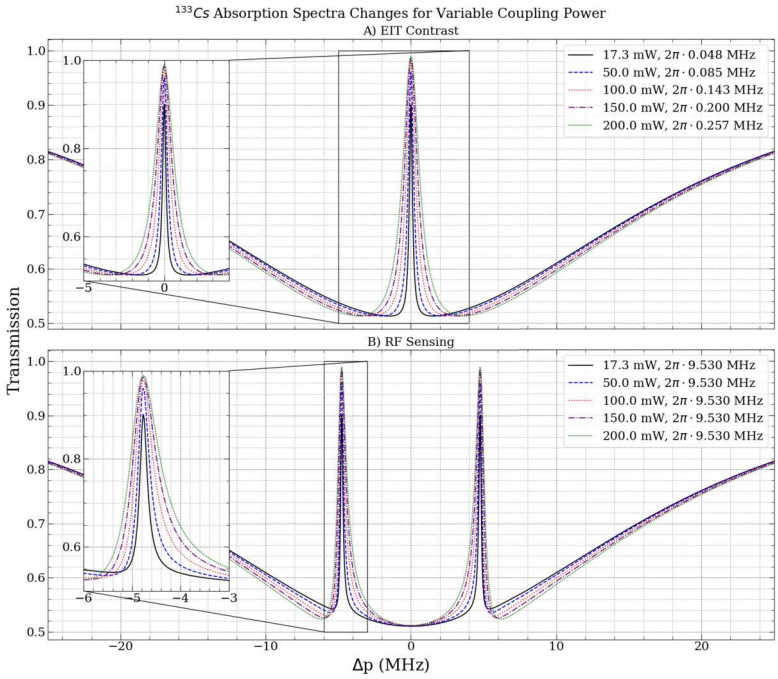


**Figure 7** Shows changes in the probe spectra when the probe power is kept constant at 3.2 $\mu$W. A) Shows how the EIT contrast change in relation to the changes in the coupling laser power. B) How the effect the change in coupling power has when monitoring the splitting introduced by the presence of a 0.75 V m$^{-1}$ RF field. (the solid black curve is generated using the experimental parameters shown in [48])

we can start to see the effect increasing the probe power has on both the EIT linewidth broadening and this reduces the accuracy of the RF sensing.

Figure 7 shows how increasing the coupling power affects the EIT contrast in A) and the effect this has on the RF sensing in B). By increasing the coupling power, the linewidth of the transparency window increases as expected. The transmitted intensity is also seen to increase with the coupling power increase. However there is a critical point where increasing the coupling laser power will broaden the linewidths without increasing the transmission. When looking at Fig. 7 B) there is a change in the transmitted intensity of the peak with the increase in coupling power and a broadening of the linewidth. This could have a negative impact on the capability of the sensor directly detecting weaker RF fields.

In Fig. 8 the effect of changing the RF intensity and keeping the frequency fixed is observed on the probe spectra for direct detection. By varying the RF electric field strength it is seen that the separation of the two peaks changes, with the weakest field not completely splitting the transparency window. By using Equation (11), the applied field intensity is estimated and compared to the input intensity. For the field which has not completely split the transparency window then Equation (11) still holds true with the estimated RF power at 0.052 V m$^{-1}$, The accuracy of this could be further increased by increasing the number of steps in the scan as currently this is 16.65 kHz per step.

### *4.1.2 Laser linewidth broadening*

To expand further on the work presented, the numerical model is developed to include details on laser linewidth. As shown in equations (5), laser linewidth is treated in the Lindblad super-operator meaning that this is an expansion of the collapse operator. By

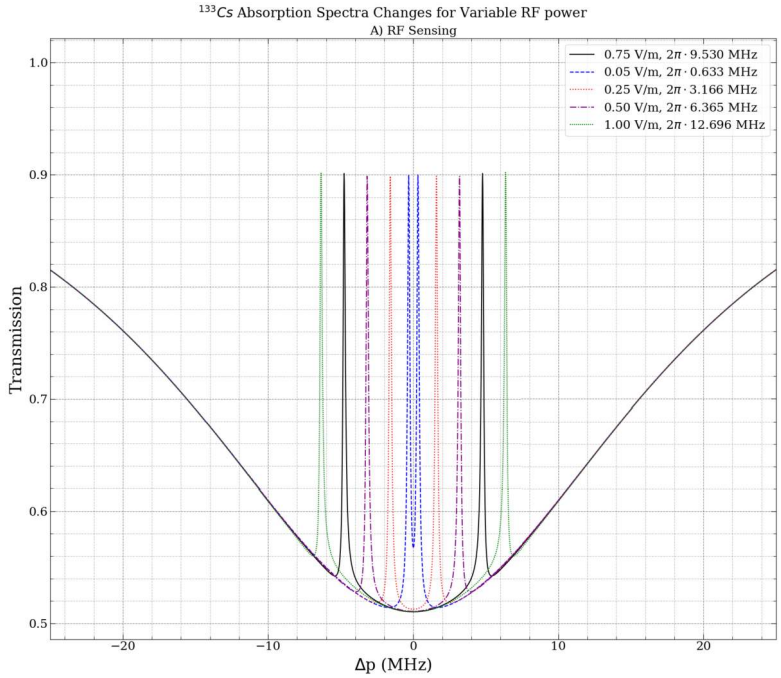


**Figure 8** Shows how changes in the RF power when the probe and coupling laser power is kept fixed to the values (3.2 $\mu$W and 17.3 mW). As the RF intensity increase the splitting in the atomic spectra increases, with the solid black line matching to the experimental parameters shown in [48]

including this it is possible to expand the model from considering monochromatic light to laser light with a finite linewidth.

Figure 9 demonstrates the effect changing the probe laser linewidth has on the transmission spectra for each stage of the RF sensor. A) show how increasing the probe laser linewidth decreases on resonant absorbance and increase the full width half maximum (FWHM) B) When the coupling laser is applied to the system, two effects are seen. Firstly, as the probe laser linewidth increases the intensity of the transparency window decreases. The second effect is the FWHM of the transparency window increases as the probe linewidth increases. C) The RF sensor begins to lose sensitivity as the probe laser linewidth increases. So ideally having a tight linewidth for the probe will result in an increase in sensitivity for direct RF detection.

Figures 10 A) show the effect the coupling laser linewidth has, similar to that of the probe laser, as the linewidth increases the EIT FWHM increases and the intensity of light passing through reduces. B) The RF sensing is affected with a reduction in the peak intensity which can cause broadening to occur leading to a decrease in the sensitivity of the RF splitting measurement.

### *4.1.3 Off-resonance RF splitting*

In Fig. 11 the effect of frequency detuning in the RF away from the resonance is shown to increase system sensitivity, in agreement with the work presented in [19]. The first effect to notice is that the peaks are asymmetrical. The second effect is that the separation in the peaks increases the further off resonance the field is. This means to calculate the field strength Equation (11) needs to be modified to account for this change. By replacing the

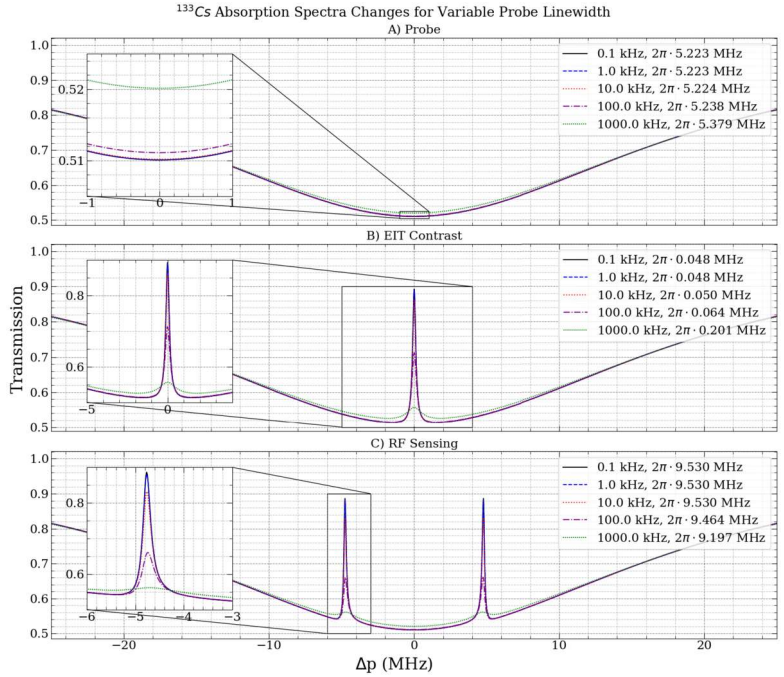


**Figure 9** A) Shows the effect of increasing the probe laser linewidth on the transmission spectra when the coupling laser linewidth is kept fixed at 1 kHz. B) Shows the effect this increasing linewidth has on the EIT contrast. C) shows the effect this has on the capability of RF sensing with increasing linewidths

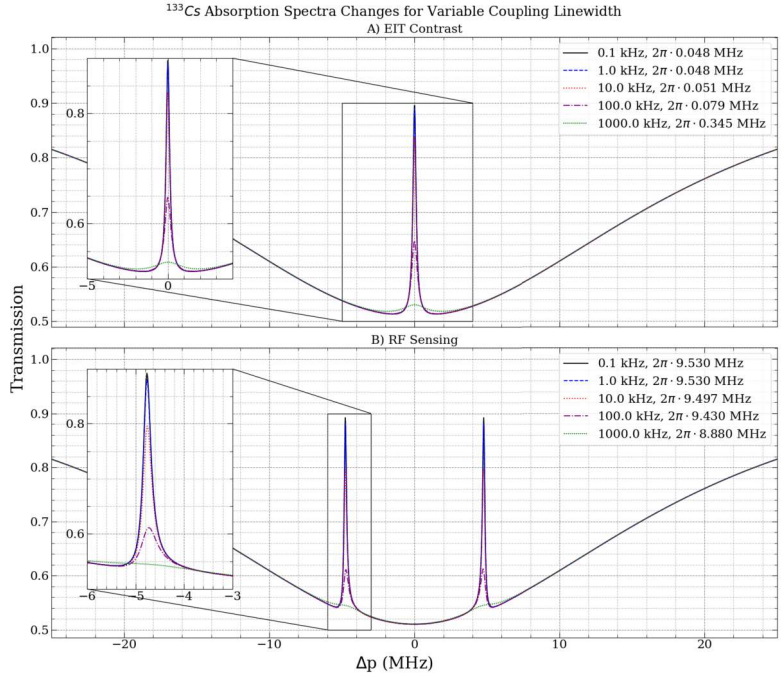


**Figure 10** A) shows the change in the EIT contrast when varying the coupling laser linewidth (with the probe linewidth kept fixed at 1 kHz). B) shows the effect this change has on the RF sensor

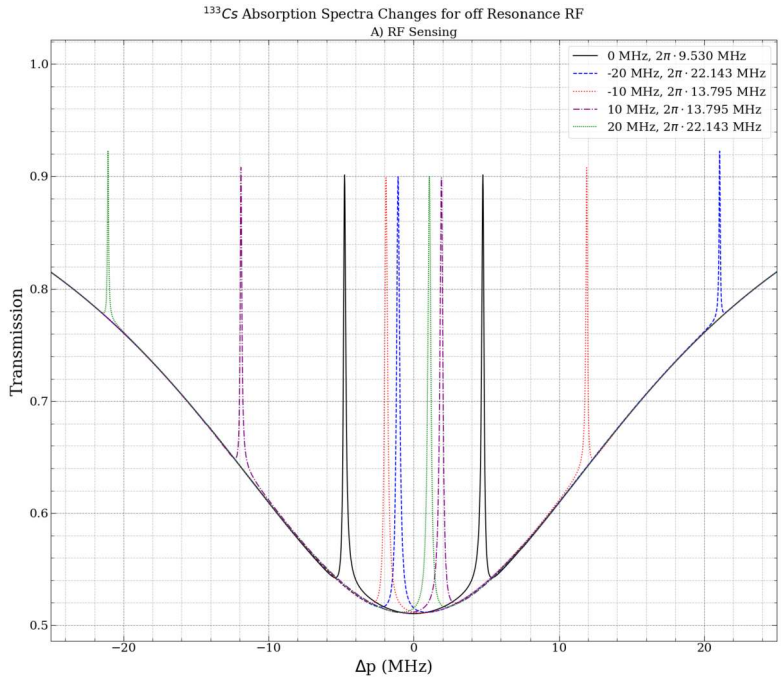


**Figure 11** Show how shifting the RF field on, and off resonance creates an asymmetry in the splitting seen in the probe spectra

$\Delta f_m$ with $\Delta f_0$ shown in Equation (12) taken from [19] equation (2) then the relative field strength can be calculated using this substitution,

$$\Delta f_0 = \sqrt{\Delta f_\delta^2 - \delta_{rf}^2} \tag{12}$$

For Equation (12) to be valid the splitting and detuning are measured in MHz. $\delta_{rf}$ is the amount the RF field is detuned from the central resonance of the RF transition. $\Delta f_\delta$ is the splitting seen in the probe spectra. Taking the value from this and substituting it in Equation (11) it is possible to calculate the applied RF intensity. For $\pm$ 10 MHz and $\pm$ 20 MHz detuning the calculated field strength is 0.747 V m$^{-1}$. Both values are within an acceptable range of the input value of 0.75 V m$^{-1}$. This RF detuning from the resonance of the transition could give an enhancement to the sensitivity of the atom-based sensor for weaker fields.

## 4.2 Transmission profiles for $^{85}$Rb

Following on from the work presented using $^{133}$Cs, the numerical model is now adapted to a different atomic species by changing the focus to $^{85}$Rb and comparing against the work presented in [19]. In a similar approach to Sect. 4.1, the model is validated against the experimental aspects of [19] and expands on that work by considering how the parameter sweep affects the system and how this can be improved. As before this is a 4-level cascade system and the atomic transitions considered are the $5S_{1/2} \rightarrow 5P_{3/2} \rightarrow 26D_{5/2} \rightarrow 27P_{3/2}$. The probe laser is a 780 nm laser which is operated at 17.5 $\mu$W with a beam waist of 0.160 mm and the coupling laser at 480 nm is set up in a counter-propagating configuration with a power of 32 mW and beam waist of 0.244 mm.

The section is split in to three. Section 4.2.1 will consider how changes in the Rabi frequency affect the System. Section 4.2.2 will look at how the laser linewidth broadening affects the sensor and Sect. 4.2.3 will look at how RF frequency detuning could increase the atomic RF sensor sensitivity for direct detection.

### *4.2.1 Rabi frequency dependencies of RF sensitivity*

Figure 12 shows the change in the atomic spectra as the different lasers and RF fields are applied to the system. In Fig. 12 A) each of the probe powers chosen give a linewidth for this transition above the value reported in [50] at $2\pi \times$ 6.069 MHz. This shows that the atomic transition is being over-saturated. This is the result of power broadening [51]. Even with this power broadening present in the probe transition, Fig. 12 B) shows the EIT window is still opened; however, depending on the intensity of the power broadening the effect of over saturating the ground to first excited state is seen, with a widening of the window and a reduction in sharpness. In Fig. 12 C) the splitting of the transparency window is seen when the RF field is applied, however as the probe power is increased the accuracy of the splitting reduces and causes an inaccuracy to appear when calculating the applied RF intensity using Equation (11).

When calculating the input RF field strength by measuring the splitting in the peaks, the splitting ranges from 23.672 MHz down to 21.22 MHz. With a dipole moment of 522.64 $a_0 e$. we find the calculated RF field strength which ranges from 3.54 V m$^{-1}$ to 3.17 V m$^{-1}$. This demonstrates the importance of keeping the probe power weak as this will have a significant effect on the RF sensor's sensitivity.

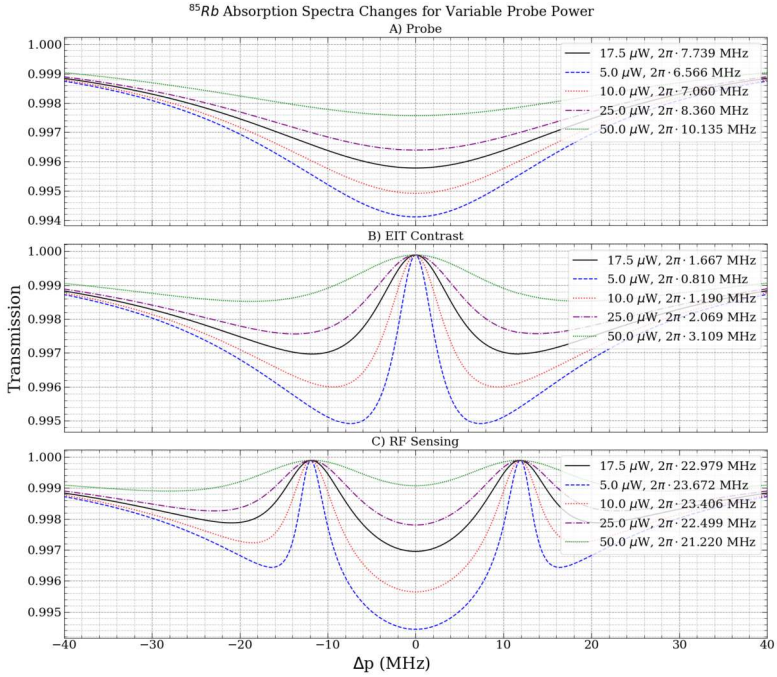


**Figure 12** A) Shows the effect of probe power on probe transmission spectra. B) EIT contrast as function of probe power (at constant coupling power of 32 mW ). C) Show the effect changes in probe power has on the RF splitting (at constant coupling power of 32 mW and constant RF field strength at 3.57 V m$^{-1}$)

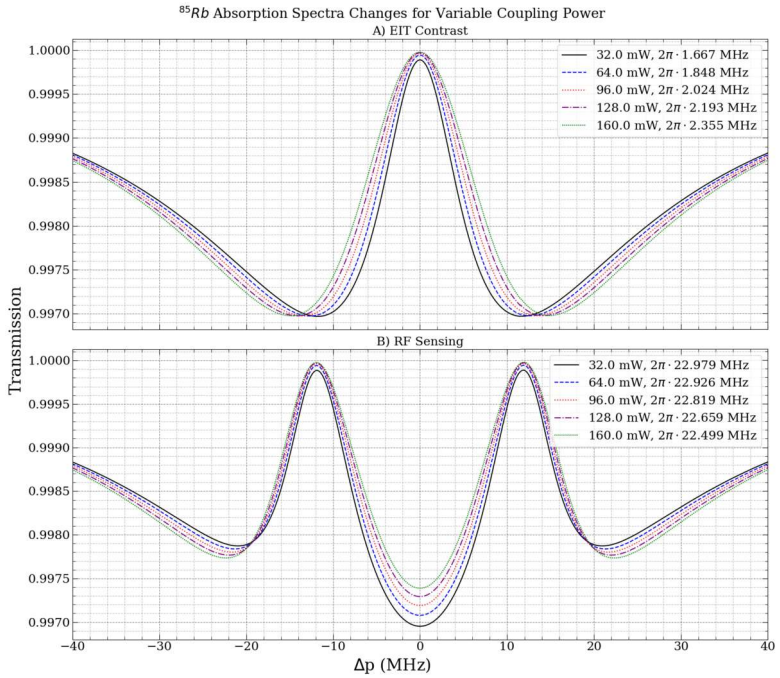


**Figure 13** Shows how the system changes when the coupling laser power is changed but the probe and RF are kept fixed (17.5 $\mu$W and 3.57 V m$^{-1}$). A) shows the change in the EIT contrast with increasing coupling power. B) Show how this effects the RF splitting

In Fig. 13 we keep the probe and RF field strength at the value stated in [19] so the system is operating over the saturation intensity. A) shows a broadening of the linewidth in the EIT contrast and a slight increase in the transmitted intensity of the 780 nm laser light. In B) the accuracy of the RF splitting decreases with the increased coupling power; this is due to the over saturation of the systems probe laser meaning the resolution of the splitting is significantly reduced.

Figure 14 shows the effect of changing the RF intensity on the probe spectra for direct RF detection. By varying the RF intensity, the separation of the two peaks changes with the weaker fields but not completely splitting the transparency window. The splitting shown gives a close approximation to the applied RF intensity and this could be further improved by either reducing the probe power or increasing the beam diameter.

### *4.2.2 Laser linewidth broadening*

Figure 15 shows how changes to the probe laser linewidth affect the capability of the RF sensor being built, although this effect is less dominant in A) as due to the power broadening there is an increase in the absorption linewidth. In B) the laser linewidth affects the intensity of the EIT window which decreases with the increase in linewidth of the probe. When operating the system as an RF sensor the laser linewidth further reduces the accuracy of the RF sensor which has already been diminished by the presence of power broadening.

In Fig. 16 the numerical model shows the effect changing the coupling laser linewidth has on the Rydberg RF sensor. As the coupling laser linewidth increases the EIT contrast shown in Fig. 16A) shows a reduction in the transmitted probe power in the transparency

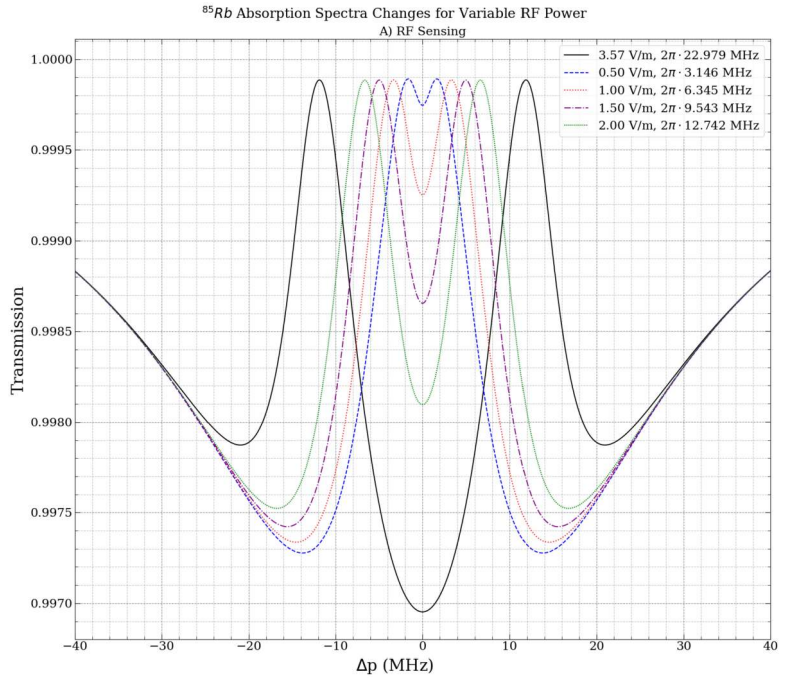


**Figure 14** Shows how changes in the RF power when the probe and coupling laser power is kept fixed (17.5 $\mu$W and 32 mW). As the RF intensity increase the splitting in the atomic spectra increases. With the green dotted line matching to the experimental parameters shown in [19]

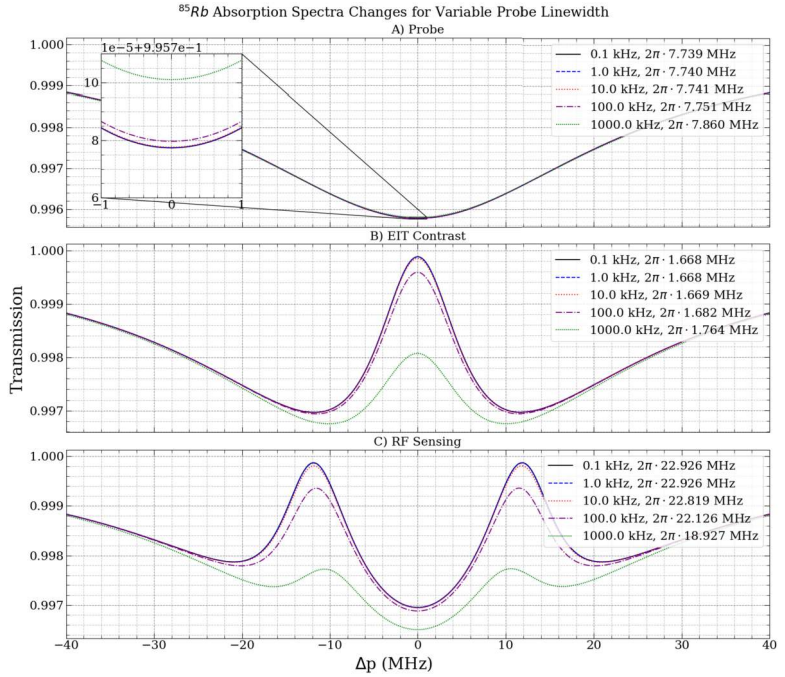


**Figure 15** Displays how changes to the laser linewidth in the probe laser affect each stage of the RF sensor. For this the laser and RF power and beam diameter are constant at the values stated above, the coupling laser linewidth is set to 1 kHz. A) the linewidth of the probe absorption increases as the laser linewidth increases. B) shows how the EIT contrast changes with increasing the probes linewidth. C) With the increasing linewidth of the probe laser reduces the accuracy of the RF sensing

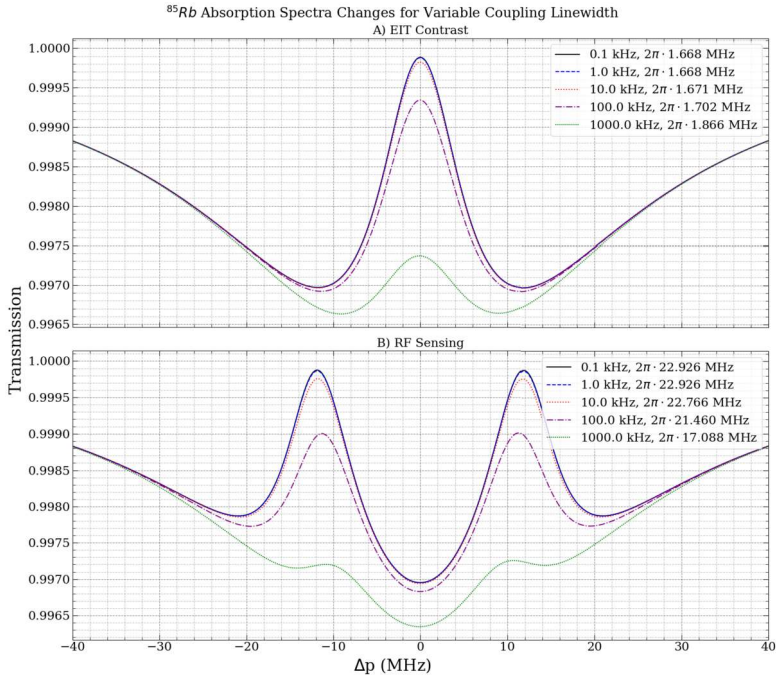


**Figure 16** Displays how changes to the laser linewidth in the coupling laser effect each stage of the RF sensor for this we kept the laser and RF power and beam diameter constant to the value stated above, the probe laser linewidth was set to 1 kHz. A) Shows how the EIT contrast changes with increasing the coupling linewidth. B) Shows the effect coupling linewidth has on the RF induced splitting

window and a slight broadening in the linewidth of the transition. In Fig. 16 B) the effect of the coupling laser linewidth reduces the RF induced splitting which consequently causes a reduction in the sensitivity when measuring the absolute power of the applied RF field.

### *4.2.3 Off-resonance RF splitting*

Figure 17 and Fig. 18 demonstrate how using RF detuning from the resonance of the transition could be used to improve the system sensitivity. In this system the probe is over saturating the atomic transition which introduces an uncertainty in the measurement of the RF amplitude. When comparing these results from these two figures to the results shown in Fig. 14 it is clear there is a strong splitting caused in Fig. 18 with the weaker RF field which was not present in Fig. 14. However, due to the detuning from resonance the splitting induced by the weakest field cannot be calculated as this results in an imaginary number from Equation (12). We are able to compare the RF field strength from 14 when the applied RF field strength is 1 V m$^{-1}$. The splitting induced by this field in our system seen in Fig. 14 is 6.345 MHz, which gives a field strength of 0.95 V m$^{-1}$. When we compare this to the off resonance splitting of Fig. 18 which gives a splitting of 20.26 MHz, the estimated field strength is 0.48 V m$^{-1}$ which is significantly lower than the on-resonance detection value. This is due to the field strength of the probe laser over saturating the transition which causes significant power broadening unlike our Cs example seen earlier.

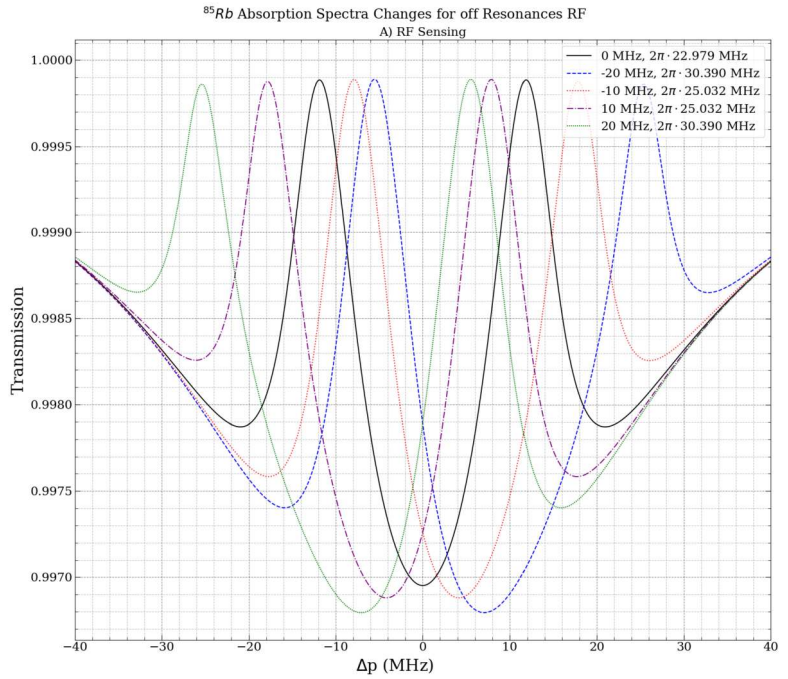


**Figure 17** Show how shifting the RF field on, and off resonance creates an asymmetry in the splitting seen in the probe spectra which can be used for enhanced sensing

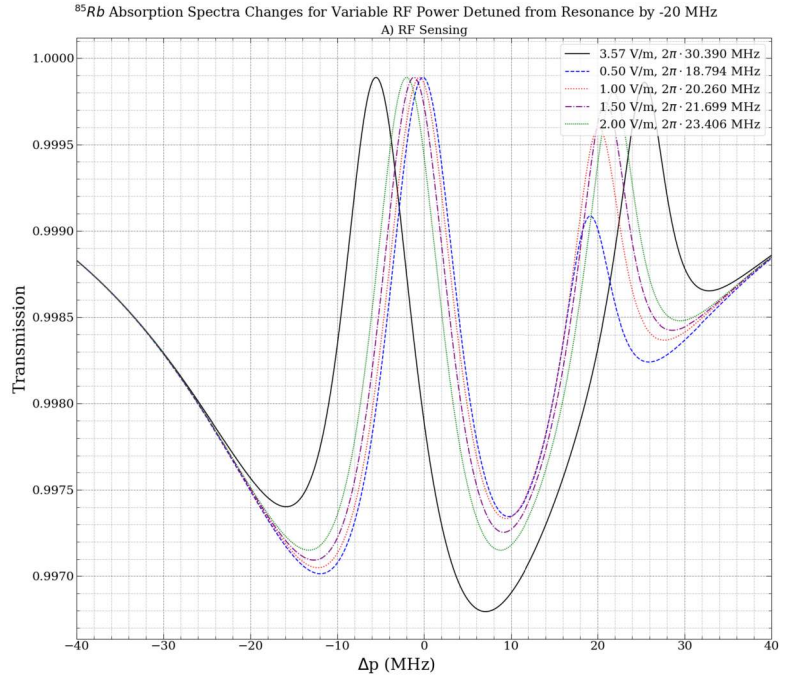


**Figure 18** Shows how shifting off resonance by -20 MHz for different RF field strengths changes probe spectra demonstrating the enhanced sensing when compared to Fig. 14

# 5 Conclusion and future work

## 5.1 Conclusion

By transitioning from a basic three-level ladder system to an N-level setup, the constraints on laser frequencies for atomic RF sensors are eased, enabling the utilization of more economical near-infrared sources. However, the complexity of optimizing an N-level system solely through experimentation proves impractical due to the multitude of parameters involved. To tackle this issue, we introduce a numerical model for analyzing N-level ladder systems in Rubidium and Caesium. Validated against independent experimental data, the model accurately reproduces observed spectra and RF-induced splitting, underscoring its reliability and guiding potential for future experiments.

This investigation explores how changes in operational parameters, such as laser linewidth and power, impact power broadening, sensor sensitivity, and bandwidth. Moreover, it demonstrates how frequency detuning of the RF from resonance can bolster system performance in directly detecting weak RF fields shown in Fig. 18. The absorption profile underlying these findings aligns with prior research on interactions within 2, 3, and 4 atomic energy level systems, with a focus on RF intensity measurement.

Harnessing this model aids in identifying the optimal operating regime to enhance sensitivity in atomic radio receivers and sensors across diverse applications within the quantum technology sector. With cost-effective near-infrared laser diodes readily available, the exploration of various N-level systems becomes feasible. This numerical model serves as a valuable tool in pinpointing operational parameters for sensitivity optimization.

## 5.2 Future work

In order to detect RF signals within current commercial 5G frequency ranges (e.g. sub 6 GHz) requires the excitation of Rydberg states with a principal atomic number in the range of n = 70 to 80. To couple between a ground state and a n = 80 Rydberg state using just two frequencies requires the use of visible lasers (e.g. 480 nm blue and 780 nm red using Rubidium). Such lasers are costly and suffer high attenuation within optical fiber, so they are not ideal for use within a fiber network. It will be much more convenient to use semiconductor lasers operating at standard telecomms wavelengths around 1300 nm and 1570 nm. However if longer wavelengths are used, then at least three-laser [52] systems will be required to reach high Rydberg states, possibly even four-laser or five-laser systems. This system offers the advantage of integration into a distributed long-range sensor network, deployable through standard single-mode fiber used in telecommunications networks. Our future work will delve deeper into this potential application within our modelling framework.

Utilizing the techniques illustrated in Figs. 11, 17 and 18 for off-resonance RF sensing can significantly enhance the sensitivity of the Rydberg receiver, particularly in weak field regimes relevant to communication and RF sensing applications. Experimental validation of these enhancements is imperative for further exploration.

In upcoming iterations of our numerical model, we aim to enhance user experience by implementing a graphical user interface, streamlining data input, and transitioning away from command line interfaces. Additionally, we plan to integrate dynamic field analysis capabilities, leveraging QuTiP libraries known for modelling dynamic systems. This extension will build upon our established steady-state model, facilitating transient solutions crucial for describing state transitions, such as those induced by amplitude modulations.

From a commercial perspective, our model holds promise for simulating communication and radar systems. Future developments will expand its scope to include hyperfine structure, enhancing state selectivity in RF detection. Moreover, we will investigate additional mechanisms of broadening, such as pressure and collisional broadening within the vapor cell, particularly pertinent as we scale down the system's vapor cell size.

**Abbreviations**
RF, Radio Frequency; SI, Internation System of Units; EIT, Electromagnetically Induced Transparency; AT Splitting, Aulter-Townes Splitting; ARC, Atomic Rydberg Calculator; FWHM, Full Width Half Maximum.

## Supplementary information

**Supplementary information** accompanies this paper at https://doi.org/10.1140/epjqt/s40507-024-00291-5.

**Additional file 1.** The authors declare that the data supporting the findings of this study are available within the paper along with the supplementary information files which contain the numerical model used in this paper. Further details on this data and model can be obtained from the corresponding authors or accessed via our github - https://github.com/Liambussey/Rydberg_RF_Sensing. (PDF 250 kB)

**Acknowledgements**
This project was supported by the Royal Commission for the Exhibition of 1851 as part of the industrial fellowship, together with the ERA foundation, BT, and the University of Birmingham. With further thanks to Professor Tim Whitley and Dr Dan Gilks for his continued support on this project and development of the numerical model.

**Author contributions**
L.B, F.B and S.W Conceptualization; Investigation; Methodology; Writing – original draft; Writing – review & editing, Data curation; Formal analysis. L.B, S.W, Y.K and Y.L Data Visualisation and Model Development L.B prepared Fig. 1-4 L.B and S.W prepared Fig. 5 - 17 Y.K , Y.L, F.B , C.C and K.B Writing – review & editing, Project management; PhD Supervision All authors reviewed the manuscript and approved the final draft for publication.

**Funding**
This project was supported by the Royal Commission for the Exhibition of 1851 as part of the industrial fellowship together with the ERA foundation.

**Data Availability**
No datasets were generated or analysed during the current study.

## Declarations

**Ethics approval and consent to participate**
Not applicable.

**Consent for publication**
The Authors of this paper have the required consent to publication.

**Competing interests**
The authors declare no competing interests.

**Author details**
[1]Applied Research, British Telecommunications, Adastral Park, Ipswich, IP5 3RE, Suffolk, UK. [2]School of Physics and Astronomy, University of Birmingham, Edgbaston Park, Birmingham, B15 2TT, UK. [3]Department of Electronic, Electrical and Systems Engineering, University of Birmingham, Edgbaston, Birmingham, B15 2TT, UK. [4]Quantum Technologies, German Aerospace Center, Wilhelm Rugne Straße, Ulm, 89081, Germany.

Received: 9 May 2024 Accepted: 6 November 2024 Published online: 18 November 2024

**References**

1. Holloway CL, Simons MT, Gordon JA, Dienstfrey A, Anderson DA, Raithel G. Electric field metrology for SI traceability: systematic measurement uncertainties in electromagnetically induced transparency in atomic vapor. J Appl Phys. 2017;121(23):233106. https://doi.org/10.1063/1.4984201.
2. Downes LA, Torralbo-Campo L, Weatherill KJ. A practical guide to terahertz imaging using thermal atomic vapour. New J Phys. 2023;25(3):035002. https://doi.org/10.1088/1367-2630/acb80c.
3. Menchetti M, Bussey LW, Gilks D, Whitley T, Constantinou C, Bongs K. Digitally encoded RF to optical data transfer using excited Rb without the use of a local oscillator. J Appl Phys. 2023;133(1):014401. https://doi.org/10.1063/5.0129107.

4. Bussey LW, Winterburn A, Menchetti M, Burton F, Rydberg WT. RF receiver operation to track RF signal fading and frequency drift. J Lightwave Technol. 2021. 1–1. https://doi.org/10.1109/jlt.2021.3098348.
5. Holloway CL, Gordon JA, Jefferts S, Schwarzkopf A, Anderson DA, Miller SA, et al. Broadband Rydberg atom-based electric-field probe for SI-traceable, self-calibrated measurements. IEEE Trans Antennas Propag. 2014;62(12):6169–82. https://doi.org/10.1109/tap.2014.2360208.
6. Holloway CL, Simons MT, Haddab AH, Williams CJ, Holloway MW. A "real-time" guitar recording using Rydberg atoms and electromagnetically induced transparency: quantum physics meets music. AIP Adv. 2019;9(6):065110. https://doi.org/10.1063/1.5099036.
7. Bussey LW, Burton FA, Bongs K, Goldwin J, Whitley T. Quantum shot noise limit in a Rydberg RF receiver compared to thermal noise limit in a conventional receiver. IEEE Sens Lett. 2022. 1–4. https://doi.org/10.1109/lsens.2022.3203465.
8. Prajapati N, Rotunno AP, Berweger S, Simons MT, Artusio-Glimpse AB, Voran SD, et al. TV and video game streaming with a quantum receiver: a study on a Rydberg atom-based receiver's bandwidth and reception clarity. AVS Quantum Sci. 2022;4(3):035001. https://doi.org/10.1116/5.0098057.
9. Meyer DH, O'Brien C, Fahey DP, Cox KC, Kunz PD. Optimal atomic quantum sensing using electromagnetically-induced-transparency readout. Phys Rev a. 2021;104(4). https://doi.org/10.1103/physreva.104.043103.
10. Meyer DH, Cox KC, Fatemi FK, Kunz PD. Digital communication with Rydberg atoms and amplitude-modulated microwave fields. Appl Phys Lett. 2018;112(21):211108. https://doi.org/10.1063/1.5028357.
11. Simons MT, Haddab AH, Gordon JA, Holloway CL. A Rydberg atom-based mixer: measuring the phase of a radio frequency wave. Appl Phys Lett. 2019;114(11):114101. https://doi.org/10.1063/1.5088821.
12. Song Z, Liu H, Liu X, Zhang W, Zou H, Zhang J, et al. Rydberg-atom-based digital communication using a continuously tunable radio-frequency carrier. Opt Express. 2019;27(6):8848–57. https://doi.org/10.1364/OE.27.008848.
13. Downes LA, Mackellar AR, Whiting DJ, Bourgenot C, Adams CS, Weatherill KJ. Full-Field Terahertz Imaging at Kilohertz Frame Rates Using Atomic Vapor. Phys Rev X. 2020;**10**(1). https://doi.org/10.1103/physrevx.10.011027.
14. Artusio-Glimpse A, Simons MT, Prajapati N, Holloway CL. Modern RF measurements with hot atoms: a technology review of Rydberg atom-based radio frequency field sensors. IEEE Microw Mag. 2022;23(5):44–56. https://doi.org/10.1109/MMM.2022.3148705.
15. Otto JS, Hunter MK, Kjærgaard N, Deb AB. Data capacity scaling of a distributed Rydberg atomic receiver array. J Appl Phys. 2021;129(15):154503. https://doi.org/10.1063/5.0048415.
16. Kumar S, Fan H, Kübler H, Sheng J, Shaffer JP. Atom-based sensing of weak radio frequency electric fields using homodyne readout. Sci Rep. 2017;7(1):42981. https://doi.org/10.1038/srep42981.
17. Jing M, Hu Y, Ma J, Zhang H, Zhang L, Xiao L, et al. Atomic superheterodyne receiver based on microwave-dressed Rydberg spectroscopy. Nat Phys. 2020;16(9):911–5. https://doi.org/10.1038/s41567-020-0918-5.
18. Holloway CL, Simons MT, Gordon JA, Wilson PF, Cooke CM, Anderson DA, et al. Atom-based RF electric field metrology: from self-calibrated measurements to subwavelength and near-field imaging. IEEE Trans Electromagn Compat. 2017;59(2):717–28. https://doi.org/10.1109/temc.2016.2644616.
19. Simons MT, Gordon JA, Holloway CL, Anderson DA, Miller SA, Raithel G. Using frequency detuning to improve the sensitivity of electric field measurements via electromagnetically induced transparency and Autler-Townes splitting in Rydberg atoms. Appl Phys Lett. 2016;108(17):174101. https://doi.org/10.1063/1.4947231.
20. Kumar S, Fan H, Kübler H, Jahangiri AJ, Shaffer JP. Rydberg-atom based radio-frequency electrometry using frequency modulation spectroscopy in room temperature vapor cells. Opt Express. 2017;25(8):8625–37. https://doi.org/10.1364/OE.25.008625.
21. Santamaria-Botello G, Verploegh S, Bottomley E, Popovic Z. Comparison of Noise Temperature of Rydberg-Atom and Electronic Microwave Receivers. Available from https://arxiv.org/abs/2209.00908.
22. Holloway CL, Prajapati N, Artusio-Glimpse AB, Berweger S, Simons MT, Kasahara Y, et al. Rydberg atom-based field sensing enhancement using a split-ring resonator. Appl Phys Lett. 2022;120(20):204001. https://doi.org/10.1063/5.0088532.
23. Mauger S, Millen J, Jones MPA. Spectroscopy of strontium Rydberg states using electromagnetically induced transparency. J Phys B, At Mol Opt Phys. 2007;40(22):F319–25. https://doi.org/10.1088/0953-4075/40/22/f03.
24. Simons MT, Gordon JA, Holloway CL. Simultaneous use of Cs and Rb Rydberg atoms for dipole moment assessment and RF electric field measurements via electromagnetically induced transparency. J Appl Phys. 2016;120(12):123103. https://doi.org/10.1063/1.4963106.
25. Harris SE. Lasers without inversion: interference of lifetime-broadened resonances. Phys Rev Lett. 1989;62(9):1033–6. https://doi.org/10.1103/PhysRevLett.62.1033. PRL.
26. Harris SE, Field J, Imamoğlu A. Nonlinear optical processes using electromagnetically induced transparency. Phys Rev Lett. 1990;64(10):1107.
27. Boller KJ, Imamoğlu A, Harris SE. Observation of electromagnetically induced transparency. Phys Rev Lett. 1991;66(20):2593–6. https://doi.org/10.1103/PhysRevLett.66.2593. PRL.
28. Gordon JA, Holloway CL, Schwarzkopf A, Anderson DA, Miller S, Thaicharoen N, et al. Millimeter wave detection via Autler-Townes splitting in rubidium Rydberg atoms. Appl Phys Lett. 2014;105(2):024104. https://doi.org/10.1063/1.4890094.
29. Autler SH, Townes CH. Stark effect in rapidly varying fields. Phys Rev. 1955;100(2):703–22. https://doi.org/10.1103/physrev.100.703.
30. Dawes AMC. Undergraduate Quantum Mechanics: a Numerical Approach using QuTiP. arXiv pre-print server. 2019. arXiv:1909.13651.
31. Johansson JR, Nation PD, Nori F. QuTiP 2: a Python framework for the dynamics of open quantum systems. Comput Phys Commun. 2013;184(4):1234–40. https://doi.org/10.1016/j.cpc.2012.11.019.
32. Šibalić N, Pritchard JD, Adams CS, Weatherill KJ. ARC: an open-source library for calculating properties of alkali Rydberg atoms. Comput Phys Commun. 2017;220:319–31. https://doi.org/10.1016/j.cpc.2017.06.015.
33. Robertson EJ, Šibalić N, Potvliege RM, Jones MPA. ARC 3.0: an expanded Python toolbox for atomic physics calculations. Comput Phys Commun. 2021. 261. https://doi.org/10.1016/j.cpc.2020.107814.

34. Fleischhauer M, Imamoglu A, Marangos JP. Electromagnetically induced transparency: optics in coherent media. Rev Mod Phys. 2005;77:633–73. https://doi.org/10.1103/RevModPhys.77.633.
35. Butcher PN, Cotter D. The elements of nonlinear optics. Cambridge studies in modern optics. Cambridge: Cambridge University Press; 1990.
36. Hanley RK, Bounds AD, Huillery P, Keegan NC, Faoro R, Bridge EM, et al. Probing interactions of thermal Sr Rydberg atoms using simultaneous optical and ion detection. J Phys B, At Mol Opt Phys. 2017;50(11):115002. https://doi.org/10.1088/1361-6455/aa6e79.
37. Griffiths DJ. Introduction to electrodynamics. Upper Saddle River: Pearson Education; 2014. Available from https://books.google.co.uk/books?id=J9ygBwAAQBAJ.
38. Berman PR, Malinovsky VS. Principles of laser spectroscopy and quantum optics. Princeton: Princeton University Press; 2011. Available from http://www.jstor.org/stable/j.ctvcm4gsw.
39. Zentile MA, Keaveney J, Weller L, Whiting DJ, Adams CS, ElecSus HIG. A program to calculate the electric susceptibility of an atomic ensemble. Comput Phys Commun. 2015;189:162–74. https://doi.org/10.1016/j.cpc.2014.11.023.
40. Riesch M, Jirauschek C. mbsolve: an open-source solver tool for the Maxwell-Bloch equations. Comput Phys Commun. 2021;268:108097. https://doi.org/10.1016/j.cpc.2021.108097.
41. Ogden TP. MaxwellBloch: a Python package for solving the coupled Maxwell-Bloch equations describing the nonlinear propagation of near-resonant light through thermal quantised systems such as atomic vapors. [Computer Program]. Available from https://github.com/tpogden/maxwellbloch.
42. Downes L. Simple Python tools for modelling few-level atom-light interactions. J Phys B, At Mol Opt Phys. 2023;56(22). https://doi.org/10.1088/1361-6455/acee3.
43. Barrett TD. rb-cqed: rubidium Cavity QED Simulations. GitHub repository. https://github.com/tomdbar/rb-cqed.
44. Bruvelis R. Hyperfine Transition Dynamics of D2 Line Using 4-level System Hamiltonian and QuTiP. Available from https://github.com/bruvelis/thesis/blob/master/notebooks/4-level-system/Hyperfine%20transition%20dynamics%20of%20D2%20line%20using%204-level%20system%20Hamiltonian%20and%20QuTiP.pdf.
45. Harris CR, Millman KJ, Van Der Walt SJ, Gommers R, Virtanen P, Cournapeau D, et al. Array programming with NumPy. Nature. 2020;585(7825):357–62. https://doi.org/10.1038/s41586-020-2649-2.
46. Virtanen P, Gommers R, Oliphant TE, Haberland M, Reddy T, Cournapeau D, et al. SciPy 1.0: fundamental algorithms for scientific computing in Python. Nat Methods. 2020;17(3):261–72. https://doi.org/10.1038/s41592-019-0686-2.
47. Pitchford A, Grenade C, Grimsmo A, Nation PD, Johansson JR. Master Equation Solver - QuTiP 4.5 Documentation 2020. Available from https://qutip.org/docs/4.5/guide/dynamics/dynamics-master.html?highlight=collapse.
48. Matthew S, Marcus K, Abdulaziz H, Joshua G, Christopher H, Thomas C. Rydberg atom-based RF power measurements. In: 2018 Antenna Measurement Techniques Association Symposium (AMTA). Antenna Measurement Techniques Association Symposium (AMTA). Williamsburg, VA. 2018.
49. Steck DA. Cesium D Line Data. Extensive, periodically updated compilation of atomic data relevant to quantum optics and atom optics experiments involving cesium, along with a thorough and consistent theoretical framework for the tabulated quantities. 2020. Available from http://steck.us/alkalidata.
50. Steck DA. Rubidium 85 D Line Data. 2020. Available from. http://steck.us/alkalidata; .
51. Bassett L. Quantum mechanics with applications to nanotechnology and information science. Phys Today. 2014;67(7):50. https://doi.org/10.1063/pt.3.2451.
52. You SH, Cai MH, Zhang SS, Xu ZS, Liu HP. Microwave-field sensing via electromagnetically induced absorption of Rb irradiated by three-color infrared lasers. Opt Express. 2022;30(10):16619. https://doi.org/10.1364/oe.454433.


## Publisher's Note